



KEK Preprint 2002-70

Belle Preprint 2002-24

Charmless Hadronic Two-Body B Meson Decays ^{*}

The Belle Collaboration

Abstract

We report the results of a study of two-body B meson decays to the complete set of $K\pi$, $\pi\pi$, and $K\bar{K}$ final states. The study is performed on a data sample of 31.7 ± 0.3 million $B\bar{B}$ events recorded on the $\Upsilon(4S)$ resonance by the Belle experiment at KEKB. We observe significant signals in all $K\pi$ final states and in the $\pi^+\pi^-$ and $\pi^+\pi^0$ final states. We set limits on the $\pi^0\pi^0$ and $K\bar{K}$ final states. A search is performed for partial-rate asymmetries between conjugate states for flavor-specific final states.

Typeset using REVTeX

^{*}Submitted to PRD.

(The Belle Collaboration)

B. C. K. Casey⁸, K. Abe⁹, T. Abe⁴⁴, I. Adachi⁹, Byoung Sup Ahn¹⁶, H. Aihara⁴⁵,
M. Akatsu²³, Y. Asano⁵⁰, T. Aso⁴⁹, V. Aulchenko², T. Aushev¹³, A. M. Bakich⁴⁰, Y. Ban³⁴,
A. Bay¹⁹, I. Bedny², P. K. Behera⁵¹, I. Bizjak¹⁴, A. Bondar², A. Bozek²⁸, M. Bračko^{21,14},
J. Brodzicka²⁸, T. E. Browder⁸, P. Chang²⁷, Y. Chao²⁷, K.-F. Chen²⁷, B. G. Cheon³⁹,
R. Chistov¹³, S.-K. Choi⁷, Y. Choi³⁹, Y. K. Choi³⁹, M. Danilov¹³, L. Y. Dong¹¹,
J. Dragic²², S. Eidelman², V. Eiges¹³, Y. Enari²³, F. Fang⁸, C. Fukunaga⁴⁷, N. Gabyshev⁹,
A. Garmash^{2,9}, T. Gershon⁹, B. Golob^{20,14}, A. Gordon²², R. Guo²⁵, J. Haba⁹, F. Handa⁴⁴,
T. Hara³², N. C. Hastings²², H. Hayashii²⁴, M. Hazumi⁹, E. M. Heenan²², I. Higuchi⁴⁴,
T. Higuchi⁴⁵, L. Hinz¹⁹, Y. Hoshi⁴³, W.-S. Hou²⁷, S.-C. Hsu²⁷, H.-C. Huang²⁷, T. Igaki²³,
Y. Igarashi⁹, T. Iijima²³, K. Inami²³, A. Ishikawa²³, R. Itoh⁹, H. Iwasaki⁹, Y. Iwasaki⁹,
H. K. Jang³⁸, J. H. Kang⁵⁴, J. S. Kang¹⁶, N. Katayama⁹, H. Kawai³, Y. Kawakami²³,
N. Kawamura¹, H. Kichimi⁹, D. W. Kim³⁹, Heejong Kim⁵⁴, H. J. Kim⁵⁴, Hyunwoo Kim¹⁶,
T. H. Kim⁵⁴, K. Kinoshita⁵, S. Korpar^{21,14}, P. Križan^{20,14}, P. Krokovny², R. Kulasiri⁵,
S. Kumar³³, A. Kuzmin², Y.-J. Kwon⁵⁴, J. S. Lange^{6,35}, G. Leder¹², S. H. Lee³⁸, J. Li³⁷,
R.-S. Lu²⁷, J. MacNaughton¹², G. Majumder⁴¹, F. Mandl¹², D. Marlow³⁵, T. Matsuishi²³,
S. Matsumoto⁴, T. Matsumoto⁴⁷, K. Miyabayashi²⁴, Y. Miyabayashi²³, H. Miyata³⁰,
G. R. Moloney²², T. Mori⁴, A. Murakami³⁶, T. Nagamine⁴⁴, Y. Nagasaka¹⁰,
T. Nakadaira⁴⁵, E. Nakano³¹, M. Nakao⁹, J. W. Nam³⁹, Z. Natkaniec²⁸, S. Nishida¹⁷,
O. Nitoh⁴⁸, S. Noguchi²⁴, T. Nozaki⁹, S. Ogawa⁴², T. Ohshima²³, T. Okabe²³, S. Okuno¹⁵,
S. L. Olsen⁸, Y. Onuki³⁰, W. Ostrowicz²⁸, H. Ozaki⁹, H. Palka²⁸, C. W. Park¹⁶, H. Park¹⁸,
L. S. Peak⁴⁰, J.-P. Perroud¹⁹, M. Peters⁸, L. E. Piilonen⁵², N. Root², M. Rozanska²⁸,
K. Rybicki²⁸, H. Sagawa⁹, S. Saitoh⁹, Y. Sakai⁹, H. Sakamoto¹⁷, M. Satapathy⁵¹,
A. Satpathy^{9,5}, O. Schneider¹⁹, S. Schrenk⁵, C. Schwanda^{9,12}, S. Semenov¹³, K. Senyo²³,
R. Seuster⁸, M. E. Sevier²², H. Shibuya⁴², B. Shwartz², J. B. Singh³³, N. Soni³³,
S. Stanič^{50,*}, M. Starič¹⁴, A. Sugi²³, A. Sugiyama²³, K. Sumisawa⁹, T. Sumiyoshi⁴⁷,
K. Suzuki⁹, S. Suzuki⁵³, S. Y. Suzuki⁹, T. Takahashi³¹, F. Takasaki⁹, N. Tamura³⁰,
J. Tanaka⁴⁵, M. Tanaka⁹, G. N. Taylor²², Y. Teramoto³¹, S. Tokuda²³, M. Tomoto⁹,
T. Tomura⁴⁵, K. Trabelsi⁸, T. Tsuboyama⁹, T. Tsukamoto⁹, S. Uehara⁹, K. Ueno²⁷,
Y. Unno³, S. Uno⁹, Y. Ushiroda⁹, G. Varner⁸, K. E. Varvell⁴⁰, C. C. Wang²⁷,
C. H. Wang²⁶, J. G. Wang⁵², M.-Z. Wang²⁷, Y. Watanabe⁴⁶, E. Won¹⁶, B. D. Yabsley⁵²,
Y. Yamada⁹, A. Yamaguchi⁴⁴, Y. Yamashita²⁹, M. Yamauchi⁹, H. Yanai³⁰, M. Yokoyama⁴⁵,
Y. Yuan¹¹, Y. Yusa⁴⁴, Z. P. Zhang³⁷, V. Zhilich², and D. Žontar⁵⁰

¹Aomori University, Aomori

²Budker Institute of Nuclear Physics, Novosibirsk

³Chiba University, Chiba

⁴Chuo University, Tokyo

- ⁵University of Cincinnati, Cincinnati OH
- ⁶University of Frankfurt, Frankfurt
- ⁷Gyeongsang National University, Chinju
- ⁸University of Hawaii, Honolulu HI
- ⁹High Energy Accelerator Research Organization (KEK), Tsukuba
- ¹⁰Hiroshima Institute of Technology, Hiroshima
- ¹¹Institute of High Energy Physics, Chinese Academy of Sciences, Beijing
- ¹²Institute of High Energy Physics, Vienna
- ¹³Institute for Theoretical and Experimental Physics, Moscow
- ¹⁴J. Stefan Institute, Ljubljana
- ¹⁵Kanagawa University, Yokohama
- ¹⁶Korea University, Seoul
- ¹⁷Kyoto University, Kyoto
- ¹⁸Kyungpook National University, Taegu
- ¹⁹Institut de Physique des Hautes Énergies, Université de Lausanne, Lausanne
- ²⁰University of Ljubljana, Ljubljana
- ²¹University of Maribor, Maribor
- ²²University of Melbourne, Victoria
- ²³Nagoya University, Nagoya
- ²⁴Nara Women's University, Nara
- ²⁵National Kaohsiung Normal University, Kaohsiung
- ²⁶National Lien-Ho Institute of Technology, Miao Li
- ²⁷National Taiwan University, Taipei
- ²⁸H. Niewodniczanski Institute of Nuclear Physics, Krakow
- ²⁹Nihon Dental College, Niigata
- ³⁰Niigata University, Niigata
- ³¹Osaka City University, Osaka
- ³²Osaka University, Osaka
- ³³Panjab University, Chandigarh
- ³⁴Peking University, Beijing
- ³⁵RIKEN BNL Research Center, Brookhaven NY
- ³⁶Saga University, Saga
- ³⁷University of Science and Technology of China, Hefei
- ³⁸Seoul National University, Seoul
- ³⁹Sungkyunkwan University, Suwon
- ⁴⁰University of Sydney, Sydney NSW
- ⁴¹Tata Institute of Fundamental Research, Bombay
- ⁴²Toho University, Funabashi

⁴³Tohoku Gakuin University, Tagajo

⁴⁴Tohoku University, Sendai

⁴⁵University of Tokyo, Tokyo

⁴⁶Tokyo Institute of Technology, Tokyo

⁴⁷Tokyo Metropolitan University, Tokyo

⁴⁸Tokyo University of Agriculture and Technology, Tokyo

⁴⁹Toyama National College of Maritime Technology, Toyama

⁵⁰University of Tsukuba, Tsukuba

⁵¹Utkal University, Bhubaneswer

⁵²Virginia Polytechnic Institute and State University, Blacksburg VA

⁵³Yokkaichi University, Yokkaichi

⁵⁴Yonsei University, Seoul

*on leave from Nova Gorica Polytechnic, Slovenia

I. INTRODUCTION

There exists a gold mine of weak and hadronic physics in two-body B meson decays to the $K\pi$, $\pi\pi$, and $K\bar{K}$ final states. Indeed, if one assumes unitarity of the quark mixing matrix [1], these modes contain enough information to measure all angles of the Unitarity Triangle [2]. Methods to extract weak-sector physics from these decays are complicated by hadronic uncertainties. However, if enough final states are measured, we will have sufficient information to constrain the sizes of hadronic amplitudes and strong phases, a necessity in disentangling the unitarity angles from measurements of flavor asymmetries and the relative size of the partial widths among these modes [3–10].

We have previously reported measurements of, or limits on, the branching fractions of B mesons to the $K\pi$, $\pi\pi$, and $K\bar{K}$ final states excluding the $\pi^0\pi^0$ and $K^0\bar{K}^0$ final states [11] as well as a search for charge asymmetries in the flavor-specific $K\pi$ final states [12], based on a data sample of 11.1 million $B\bar{B}$ events. The results presented here include the previous data and supersede all previous results. Similar studies have been performed by other experiments [13–20].

Here, we present measurements of, or limits on, the branching fractions of B mesons to the $K\pi$, $\pi\pi$, and $K\bar{K}$ final states including all combinations of charged and neutral kaons and pions. We refer to these final states collectively as $B \rightarrow hh$, including charge conjugate states unless explicitly stated. For final states where the charge of the kaon or pion specifies the flavor of the parent B meson, known as flavor-specific final states, we present limits on the partial-rate asymmetries defined as

$$\mathcal{A}_{\text{CP}}(f) = \frac{N(\bar{B} \rightarrow \bar{f}) - N(B \rightarrow f)}{N(\bar{B} \rightarrow \bar{f}) + N(B \rightarrow f)},$$

where B represents either a B^0 or B^+ meson, f represents a flavor-specific final state, and \bar{B} and \bar{f} are their conjugates.

II. APPARATUS AND DATA SET

The analysis is based on data taken by the Belle detector [21] at the KEKB e^+e^- storage ring [22]. The data set consists of 29.1 fb^{-1} on the $\Upsilon(4S)$ resonance corresponding to 31.7 ± 0.3 million $B\bar{B}$ events. An off-resonance data set of 4.4 fb^{-1} was taken 60 MeV below the $\Upsilon(4S)$ resonance to perform systematic studies of the continuum $e^+e^- \rightarrow q\bar{q}$ background where q is either a u , d , s , or c quark. KEKB collides 8 GeV electrons and 3.5 GeV positrons that are stored in separate rings, producing an $\Upsilon(4S)$ system that is boosted by $\gamma\beta = 0.425$ along the beam axis. In this analysis, all variables are calculated in the center-of-mass frame of the electron and positron beams unless explicitly stated.

The Belle detector is a general purpose magnetic spectrometer with a 1.5 T axial magnetic field. Charged tracks are reconstructed using a 50 layer central drift chamber (CDC) and a 3 layer double-sided Silicon vertex detector (SVD). Candidate electrons and photons are identified using an 8736 crystal CsI(Tl) calorimeter (ECL) inside the magnet. Muon and K_L^0 candidates are identified using resistive plate chambers embedded in the iron magnetic flux return (KLM). Hadron and auxiliary lepton identification is provided by an array of 1188 Silica aerogel Čerenkov threshold counters (ACC) and a barrel of 128 time-of-flight (TOF) plastic scintillator modules.

III. EVENT RECONSTRUCTION

Event triggers based on fast signals from the CDC, ECL, TOF, and KLM [21]. Hadronic events are selected using event multiplicity and total energy variables [23]. For signal events that pass all $B \rightarrow hh$ selection criteria, the triggering and hadronic event selection efficiencies range from 99% for $B^0 \rightarrow h^+h^-$ modes to 76% for the $B^0 \rightarrow \pi^0\pi^0$ final state.

Charged π and K mesons are identified by their energy loss (dE/dx) in the CDC and their Čerenkov light yield in the ACC. For each hypothesis (K or π), the dE/dx and ACC probability density functions are combined to form likelihoods, \mathcal{L}_K and \mathcal{L}_π . K and π mesons are distinguished by a cut on the likelihood ratio $\mathcal{L}_K/(\mathcal{L}_K + \mathcal{L}_\pi)$. A similar likelihood ratio including calorimeter information is used to identify electrons. All charged tracks that originate from the interaction point and are not positively identified as electrons are considered as kaon or pion candidates.

Candidate K_S^0 mesons are reconstructed using pairs of oppositely charged tracks that have an invariant mass in the range $480 \text{ MeV} < m(\pi^+\pi^-) < 516 \text{ MeV}$ [24]. The candidate must have a displaced vertex and flight direction consistent with a K_S^0 originating from the interaction point. Candidate π^0 mesons are formed from pairs of photons with an invariant mass in the range $114 \text{ MeV} < m(\gamma\gamma) < 150 \text{ MeV}$ and $E_{\gamma(\text{lab})} > 70 \text{ MeV}$. The $\pi^+\pi^-$ and $\gamma\gamma$ mass spectra are shown in Fig. 1 for $B^+ \rightarrow K_S^0 h^+$ and $h^+\pi^0$ candidates in the beam constrained mass sideband data sample defined below.

Continuum background is reduced using event shape variables. We quantify the event topology with modified Fox-Wolfram moments [25] defined as

$$h_l^{so} = \sum_{i,j} p_i p_j P_l(\cos \theta_{ij}),$$

$$h_l^{oo} = \sum_{j,k} p_j p_k P_l(\cos \theta_{jk}),$$

where i enumerates B signal candidate particles (s particles) and j and k enumerate the *remaining* particles in the event (o particles); p_i is the i th particle's momentum, and $P_l(\cos \theta_{ij})$

is the l th Legendre polynomial of the angle θ_{ij} between particles i and j . The h_l^{so} terms contain information on the correlation between the B candidate direction and the direction of the rest of the event. The odd h_l^{so} terms partially reconstruct the kinematics of the other B in the event while the even terms quantify the sphericity of the other side of the event. We create a six-variable Fisher discriminant called the Super Fox-Wolfram defined as

$$SFW = \sum_{l=2,4} \alpha_l \left(\frac{h_l^{so}}{h_0^{so}} \right) + \sum_{l=1-4} \beta_l \left(\frac{h_l^{oo}}{h_0^{oo}} \right),$$

where α_l and β_l are the Fisher coefficients.

The SFW variable is combined with the B flight direction with respect to the beam axis, $\cos \theta_B$, to form a single likelihood

$$\mathcal{L}_{B\bar{B}} = \mathcal{L}(SFW)_{B\bar{B}} \times \mathcal{L}(\cos \theta_B)_{B\bar{B}}$$

for signal and an equivalent product for continuum, $\mathcal{L}_{q\bar{q}}$. Continuum background is suppressed by cutting on the likelihood ratio

$$LR = \frac{\mathcal{L}_{B\bar{B}}}{\mathcal{L}_{B\bar{B}} + \mathcal{L}_{q\bar{q}}}.$$

These variables are shown in Fig. 2. The signal probability density functions (PDF) are derived from Monte Carlo (MC); the continuum PDFs are taken from sideband data discussed below. The SFW PDFs are modeled as the sum of a simple Gaussian and an asymmetric Gaussian [26] for both signal and continuum; the $\cos \theta_B$ PDF is modeled as a second-order polynomial for signal and is flat for continuum. We make separate requirements on LR for each mode depending on the expected background determined using sideband data. As an example, Fig. 2 shows the $B^0 \rightarrow K^+ \pi^-$ data sample before and after imposing the $LR > 0.8$ requirement.

Table I lists the reconstruction, particle identification, and continuum suppression efficiencies for each final state [28]. The reconstruction and continuum suppression efficiencies are determined using a GEANT-based MC [29]. The error in the reconstruction efficiencies are determined by embedding MC generated particles into hadronic event data and comparing the efficiencies between the embedded events and the default MC and also by measuring the relative yields of D decays to various final states. The charged track, π^0 , and K_S^0 selection criteria efficiencies are tested by measuring the D event yields before and after each cut is applied. Further comparisons are made between kinematic distributions of particles in sideband data (discussed below) and continuum MC events. Based on the results of these studies, we assign a relative systematic error in the reconstruction efficiencies of 2.5% for charged tracks, 6.3% for K_S^0 mesons and 7.3% for π^0 mesons. The relative systematic error associated with the continuum suppression cut is 4% which is determined by taking the

ratio of $B^+ \rightarrow D^0\pi^+$ yields in data after and before continuum suppression is applied and comparing to the MC efficiency. The $B^0 \rightarrow \pi^0\pi^0$ final state includes an additional relative systematic error of 10% to account for difficulties in triggering and hadronic event selection for this mode.

A critical feature of the analysis is the measurement of the particle identification efficiency and fake rate. These are determined using nearly pure samples of K and π mesons tagged using the continuum D^{*+} decay chain $D^{*+} \rightarrow D^0\pi^+$, $D^0 \rightarrow K^-\pi^+$. Figure 3 shows the $K^-\pi^+$ invariant mass distributions before and after applying PID cuts. For tracks in the $B \rightarrow hh$ signal region of $2.4 \text{ GeV} < p < 2.8 \text{ GeV}$ ($1.5 \text{ GeV} < p_{\text{lab}} < 4.5 \text{ GeV}$) the K efficiency and fake rate are $\epsilon_K = 0.86$ and $f_K = 0.086$ (true K fakes π); the π efficiency and fake rate are $\epsilon_\pi = 0.88$ and $f_\pi = 0.071$ (true π fakes K). The relative systematic errors are 2% in the efficiencies and 4% in the fake rates. These errors are directly related to the sample purity. Figure 3 also shows $B^0 \rightarrow K^+\pi^-$ and $\pi^+\pi^-$ MC events before and after applying pion identification cuts on both tracks.

IV. B RECONSTRUCTION AND YIELD EXTRACTION

To reconstruct B mesons we form two quantities: the energy difference, $\Delta E = E_B - E_{\text{beam}}$, and the beam constrained mass, $m_{bc} = \sqrt{E_{\text{beam}}^2 - p_B^2}$, where $E_{\text{beam}} = \sqrt{s}/2 = 5.29 \text{ GeV}$, and E_B and p_B are the reconstructed energy and momentum of the B candidate in the center of mass frame. These are shown in Fig. 4 for $B^{0(+)} \rightarrow K^+\pi^{-(0)}$ and $\pi^+\pi^{-(0)}$ MC. Modes containing π^0 s have a tail extending into the negative ΔE region due to shower leakage out of the back of the calorimeter and photon interactions with the material in front of the calorimeter. We calculate the energy of final state charged particles using a pion mass assumption. This shifts ΔE by -45 MeV for each charged kaon in the final state. The signal yields are extracted by a binned maximum-likelihood fit to the ΔE distribution in the region $5.271 < m_{bc} < 5.289 \text{ GeV}$ ($m_{bc} > 5.270 \text{ GeV}$ for modes containing π^0 s) and $-300 \text{ MeV} < \Delta E < 500 \text{ MeV}$. The yields are verified by fitting m_{bc} in the ΔE signal region. A sideband region of $5.2 \text{ GeV} < m_{bc} < 5.26 \text{ GeV}$ is used to study the continuum background in the ΔE distribution, while a sideband of $150 \text{ MeV} < \Delta E < 500 \text{ MeV}$ is used to study the continuum background in the m_{bc} distribution.

The ΔE fits include four components: signal, crossfeed from other mis-identified $B \rightarrow hh$ decays, continuum background, and backgrounds from multi-body and radiative charmless B decays. These are shown in Fig. 4. The crossfeed component is shifted from the signal component by 45 MeV as described above. The charmless B decay background is dominated by events where the B meson decays to an $hh\pi$ final state such as $\rho\pi$ or $f_0(980)K$ where one pion is not reconstructed. This shifts the charmless B background by at least the mass

of the missing pion. We expect no backgrounds from $b \rightarrow c$ decays based on a large MC sample.

For charged particle final states, the ΔE signal is modeled with a Gaussian. For modes containing π^0 s, the signal is modeled as the sum of a primary Gaussian and a secondary asymmetric Gaussian. The mean positions of the two are equal and the $+\Delta E$ σ of the asymmetric Gaussian is constrained to equal the σ of the primary Gaussian. The crossfeed component has an equal shape, shifted by 45 MeV for each mis-identified particle.

The widths of the ΔE signal distributions are determined using inclusive high momentum $D^0 \rightarrow K^-\pi^+$, $K^-\pi^+\pi^0$, and $D^+ \rightarrow K_S^0\pi^+$ decays after requiring the D daughter particles to have a momentum range similar to $B \rightarrow hh$ candidate particles. These distributions are shown in Fig. 5. Comparisons between the D mass widths in MC and data are used to scale the $B \rightarrow hh$ ΔE MC widths. This procedure is also used to determine the ratio of primary to secondary Gaussians for modes containing π^0 s.

The peak positions of the ΔE signal Gaussians are a function of the beam energy and the momentum scale. The beam energy is determined using the peak position of the m_{bc} distribution for the $B^+ \rightarrow D^0\pi^+$, $D^0 \rightarrow K^-\pi^+$ data sample shown in Fig. 6. The momentum scale is determined using the peak positions of the inclusive D mass spectra discussed above as well as the ΔE distribution for the $B^+ \rightarrow D^0\pi^+$ data sample also shown in Fig. 6.

The continuum background is modeled with a second-order polynomial with coefficients determined from sideband data. Figure 7 demonstrates the validity of this method by comparing the continuum ΔE background shape in on-resonance m_{bc} sideband data to the shape in the m_{bc} signal region in the off-resonance data sample. Backgrounds from charmless B decays are modeled by a smoothed MC histogram.

For all final states except $K^+\pi^0$ and $\pi^+\pi^0$, the normalizations of the four components are the only free parameters in the fits. The significance of the signal yield above background is determined by re-fitting the ΔE distribution without a signal component and comparing the maximum likelihoods of the two fits. Due to the large overlap of the signal and crossfeed components in the $K^+\pi^0$ and $\pi^+\pi^0$ signals, we perform a simultaneous fit to the $K^+\pi^0$ and $\pi^+\pi^0$ ΔE distributions constraining the crossfeed to the expected values based on the PID fake rates.

The m_{bc} distribution provides no discrimination among the three B decay components. The sum of the three components is modeled with the same functional form as the ΔE signal shapes discussed above. We parameterize the continuum background with a function that behaves like phase space near the endpoint (the ARGUS shape [27]).

V. RESULTS

Figures 8, 9, and 10 show the ΔE and m_{bc} distributions for the $K\pi$, $\pi\pi$ and $K\bar{K}$ final states, respectively. The ΔE signal yields and the significance above background are listed in Table II [30]. Using these results and the efficiencies listed in Table I, we derive the branching fractions listed in Table II based on the data sample of 31.7 million $B\bar{B}$ events [31]. In all cases, the m_{bc} fits give consistent results. The systematic error in the fitting procedure is determined by varying the parameters of the fitting functions within their errors and measuring the change in the signal yield. The deviations from the nominal yields are typically 1 to 2 events. These deviations, along with the error in the efficiencies and $N(B\bar{B})$ (1%) are added in quadrature to give the systematic error in the branching fractions. For modes with significance below 3σ [32], we report 90% confidence level upper limits [33] calculated with the efficiency and $N(B\bar{B})$ reduced by their systematic errors.

For the $K^+\pi^0/\pi^+\pi^0$ simultaneous fit, we re-fit the distributions after removing the constraints. The central values of the signal yields differ by at most 2.3 events. These deviations are also included in the systematic error.

The effects of backgrounds from charmless B decays can be demonstrated by re-fitting the ΔE distributions in the region $\Delta E > -130$ MeV without a charmless B background component. For modes with π^0 s in the final state, the yields deviate by as much as 12%, clearly indicating the need for these components in the fit. There is almost no deviation in the yields of final states that do not include a π^0 . In each fit, the measured charmless B background yield agrees with the expected values based on independent measurements of these modes. However, the errors on the fitted yields and the expected values are both large.

In Table III, we list ratios of partial widths among the $K\pi$ and $\pi\pi$ modes [31]. The correlations between the numerator and denominator are included in the systematic error calculation. The systematic error includes a 2.5% fractional error from the ratio of charged to neutral B meson lifetimes where we have used $\tau^+/\tau^0 = 1.091 \pm 0.027$ [34] to convert the ratio of branching fractions to the ratio of partial widths.

We measure partial-rate asymmetries in all measured flavor-specific modes. The ΔE distributions are shown separately for \bar{B} and B modes for the $K^\mp\pi^\pm$, $K^\pm\pi^0$, and $\pi^\mp\pi^0$ final states in Fig. 11. Figure 12 shows the corresponding distributions for the $K_S^0\pi^\mp$ final states. The fitting results and partial-rate asymmetries are listed in Table IV. Here, the 90% confidence intervals assume Gaussian statistics and are expanded linearly by the systematic error. The systematic errors are dominated by fitting systematics but also include a 1% contribution, added in quadrature, to account for possible detector-based asymmetries, as discussed below. In the $K^\mp\pi^\pm$ final states, the asymmetry is corrected by a dilution factor of 0.984 ± 0.001 , due to double misidentification of $K^+\pi^-$ as $K^-\pi^+$.

Four samples are used to verify the symmetric performance of the Belle detector for high momentum particles. An inclusive sample of tracks in the two-body decay momentum bin $2.4 \text{ GeV} < p < 2.85 \text{ GeV}$ is used for tracking efficiency tests before and after PID cuts are applied. Events in m_{bc} sideband data further test the reconstruction efficiency along with the continuum suppression cut efficiency. We also check the difference between inclusive high momentum $D^{0(+)} \rightarrow K^- \pi^+$, $K_S^0 \pi^+$, and $K^- \pi^+ \pi^0$ decays and their charge conjugates that test for asymmetries in the detector resolution. The entire reconstruction procedure is applied to the $B \rightarrow D \pi^\mp$; $D \rightarrow K^\mp \pi^\pm$, $K_S^0 \pi^\mp$, and $K^\mp \pi^\pm \pi^0$ data samples. The results are listed in Table V. The inclusive track sample yields an asymmetry in the track reconstruction efficiency of $(N(h^-) - N(h^+))/(N(h^-) + N(h^+)) = (-3.6 \pm 0.3) \times 10^{-3}$. Considering the statistical precision of the current data set, we ignore this very small asymmetry. We also see a 1.8 MeV shift between the inclusive $D^- \rightarrow K_S^0 \pi^-$ and $D^+ \rightarrow K_S^0 \pi^+$ mass peaks indicating an approximate 0.1% momentum scale difference between positive and negative tracks. This shift has been taken into account when determining the error in the peak position of the ΔE distributions for modes with odd numbers of tracks in the final state. Furthermore, as shown in the Table V, the shift does not result in an asymmetry between the efficiency to reconstruct the two flavors. All other mass and width parameters are consistent within the errors between the two flavors for the three D decay channels. Figure 13 shows the samples most relevant to the $B^\mp \rightarrow K_S^0 \pi^\mp$ final states. With the exception of the inclusive track sample, all are consistent with zero asymmetry within the error and we conclude that detector based asymmetries are below 1%.

VI. DISCUSSION AND CONCLUSIONS

We have presented measurements of the branching fractions of all $B \rightarrow K \pi$ final states and the $B \rightarrow \pi^+ \pi^-$ and $\pi^+ \pi^0$ final states. We see no significant evidence for the decays $B^0 \rightarrow \pi^0 \pi^0$ or $B \rightarrow K \bar{K}$ and set 90% confidence level upper limits on their branching fractions. Furthermore, we see no clear evidence for partial-rate asymmetries between the \bar{B} and B decay amplitudes in these modes.

The partial-rate asymmetry between $B^- \rightarrow K^0 \pi^-$ and $B^+ \rightarrow K^0 \pi^+$ of $0.46 \pm 0.15 \pm 0.02$ has a non-zero significance of 2.9σ . Since this is below 3σ , we defer claiming evidence for an asymmetry until a larger data sample is collected.

The $\Gamma(\pi^+ \pi^-)/\Gamma(K^+ \pi^-)$ and $\Gamma(\pi^+ \pi^-)/2\Gamma(\pi^+ \pi^0)$ partial width ratios are significantly below 1. This could be an indication of large destructive interference between Tree and Penguin amplitudes for the $B^0 \rightarrow \pi^+ \pi^-$ decay although theoretical uncertainties pertaining to the relative sizes of the interfering amplitudes are still large [4–6].

Knowledge of the branching fraction for $B^0 \rightarrow \pi^0 \pi^0$ is required for an isospin analysis of $B \rightarrow \pi \pi$ decays and for the extraction of the CP violation parameter $\sin 2\phi_2$ [10]. With the

present data set we set a limit of $\mathcal{B}(B^0 \rightarrow \pi^0 \pi^0) < 6.4 \times 10^{-6}$ at the 90% confidence level. If the excess of ~ 13 events is indeed due to $B^0 \rightarrow \pi^0 \pi^0$ events, the corresponding branching fraction would be $\mathcal{B}(B^0 \rightarrow \pi^0 \pi^0) = (3.2 \pm 1.5 \pm 0.7) \times 10^{-6}$.

VII. ACKNOWLEDGMENTS

We wish to thank the KEKB accelerator group for the excellent operation of the KEKB accelerator. We acknowledge support from the Ministry of Education, Culture, Sports, Science, and Technology of Japan and the Japan Society for the Promotion of Science; the Australian Research Council and the Australian Department of Industry, Science and Resources; the National Science Foundation of China under contract No. 10175071; the Department of Science and Technology of India; the BK21 program of the Ministry of Education of Korea and the CHEP SRC program of the Korea Science and Engineering Foundation; the Polish State Committee for Scientific Research under contract No. 2P03B 17017; the Ministry of Science and Technology of the Russian Federation; the Ministry of Education, Science and Sport of the Republic of Slovenia; the National Science Council and the Ministry of Education of Taiwan; and the U.S. Department of Energy.

REFERENCES

- [1] M. Kobayashi, T. Maskawa, Prog. Theor. Phys. **49**, 652 (1973).
- [2] H. Quinn, A. I. Sanda, Eur. Phys. Jour. C **15**, 628 (2000).
- [3] R. Fleischer, J. Matias, DESY 02-040, UAB-FT-523, hep-ph/0204101.
- [4] M. Gronau, J. L. Rosner, Phys. Rev. D **65**, 013004 (2002).
- [5] M. Beneke, G. Buchalla, M. Neubert, C.T. Sachrajda, Nucl. Phys. B **606**, 245 (2001).
- [6] Y.-Y. Keum, H.-N. Li, A.I. Sanda, Phys. Rev. D **63**, 054008 (2001).
- [7] W-S. Hou, K-C Yang, Phys. Rev. Lett. **84**, 4806 (2000).
- [8] D. Atwood, A. Soni, Phys. Lett. B **466**, 326 (1999).
- [9] K. Agashe, N. G. Deshpande, Phys. Lett. B **451**, 215 (1999).
- [10] M. Gronau, D. London, Phys. Rev. Lett. **65**, 3381 (1990).
- [11] Belle Collaboration, K. Abe *et al.*, Phys. Rev. Lett. **87**, 101801 (2001).
- [12] Belle Collaboration, K. Abe *et al.*, Phys. Rev. D **64**, 071101(R) (2001).
- [13] ALEPH Collaboration, D. Buskulic *et al.*, Phys. Lett. B **384**, 471 (1996).
- [14] DELPHI Collaboration, W. Adam *et al.*, Zeit. Phys. C **72**, 207 (1996).
- [15] CLEO Collaboration, D. Cronin-Hennessy *et al.*, Phys. Rev. Lett. **85**, 515 (2000).
- [16] CLEO Collaboration, S. Chen *et al.*, Phys. Rev. Lett. **85**, 525 (2000).
- [17] SLD Collaboration, K. Abe *et al.*, Phys. Rev. D **62**, 071101 (2000).
- [18] BaBar Collaboration, B. Aubert *et al.*, Phys. Rev. Lett. **87**, 151802 (2001).
- [19] CLEO Collaboration, D. M. Asner *et al.*, Phys. Rev. D **65**, 031103(R) (2002).
- [20] BaBar Collaboration, B. Aubert *et al.*, Phys. Rev. D **65**, 051502(R) (2002).
- [21] Belle Collaboration, K. Abe *et al.*, Nucl. Inst. Meth. A **479**, 117 (2002).
- [22] E. Kikutani ed. KEKB Accelerator Papers, KEK Preprint 2001-157, to be published in Nucl. Inst. Meth. A.
- [23] Belle Collaboration, K. Abe *et al.*, Phys. Rev. D **64**, 072001 (2001).
- [24] In this Letter we use units with $c = 1$ and denote both mass and momentum with the units of energy.

- [25] G. Fox, S. Wolfram, Phys. Rev. Lett. **41**, 1581 (1978).
- [26] A Gaussian distribution with a different σ above and below the mean of the Gaussian.
- [27] ARGUS Collaboration, H. Albrecht *et al.*, Phys. Lett. B **241**, 278 (1990).
- [28] The efficiencies for the $B^{+(0)} \rightarrow K^0 \pi^{+(0)}$ and $K^0 K^+$ final states are corrected by 1/2 to account for the approximately equal mixture of K_S^0 and K_L^0 states. The $B \rightarrow K^0 \bar{K}^0$ final state is corrected by 1/2 since the asymmetric $K_S^0 K_L^0$ final state is forbidden.
- [29] R. Brun *et al.*, GEANT 3.21, CERN Report No. DD/EE/84-1 (1987).
- [30] All results are presented with the statistical error first followed by the systematic error.
- [31] We assume an equal fraction of charged and neutral B meson pairs.
- [32] An upper limit is not calculated for the $B^0 \rightarrow K_S^0 \pi^0$ mode since this mode was previously reported as an observation in Ref. 11.
- [33] The 90% confidence level in the signal yield, N , is calculated by the relation $\int_0^N \mathcal{L}(n) dn = 0.9 \int_0^\infty \mathcal{L}(n) dn$.
- [34] Belle Collaboration, K. Abe *et al.*, Phys. Rev. Lett. **88**, 171801 (2002).

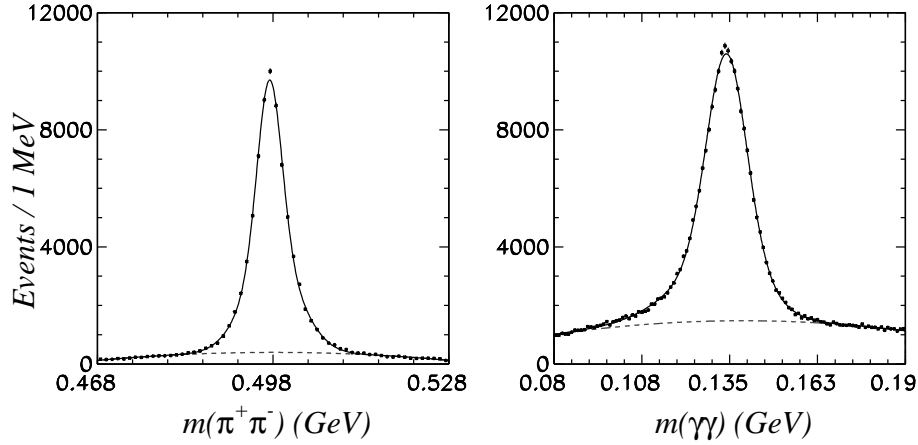


FIG. 1. The $\pi^+\pi^-$ (left) and $\gamma\gamma$ (right) mass spectra for $B^+ \rightarrow K_S^0 h^+$ and $h^+\pi^0$ candidates in the beam constrained mass sideband data sample. The $\pi^+\pi^-$ distribution is modeled as the sum of two Gaussians for true K_S^0 candidates while the background is modeled as a second-order polynomial. The weighted average resolution of the two Gaussians is 3.4 MeV for the K_S^0 mass peak. The $\gamma\gamma$ distribution is modeled as the sum of a primary symmetric Gaussian and a secondary asymmetric Gaussian [24] for π^0 candidates and a second-order polynomial for background. The weighted average resolution of the two Gaussians is 8.9 MeV for the π^0 mass peak. In both distributions the solid curves are the sum of signal and background components while the dashed curve is the background component.

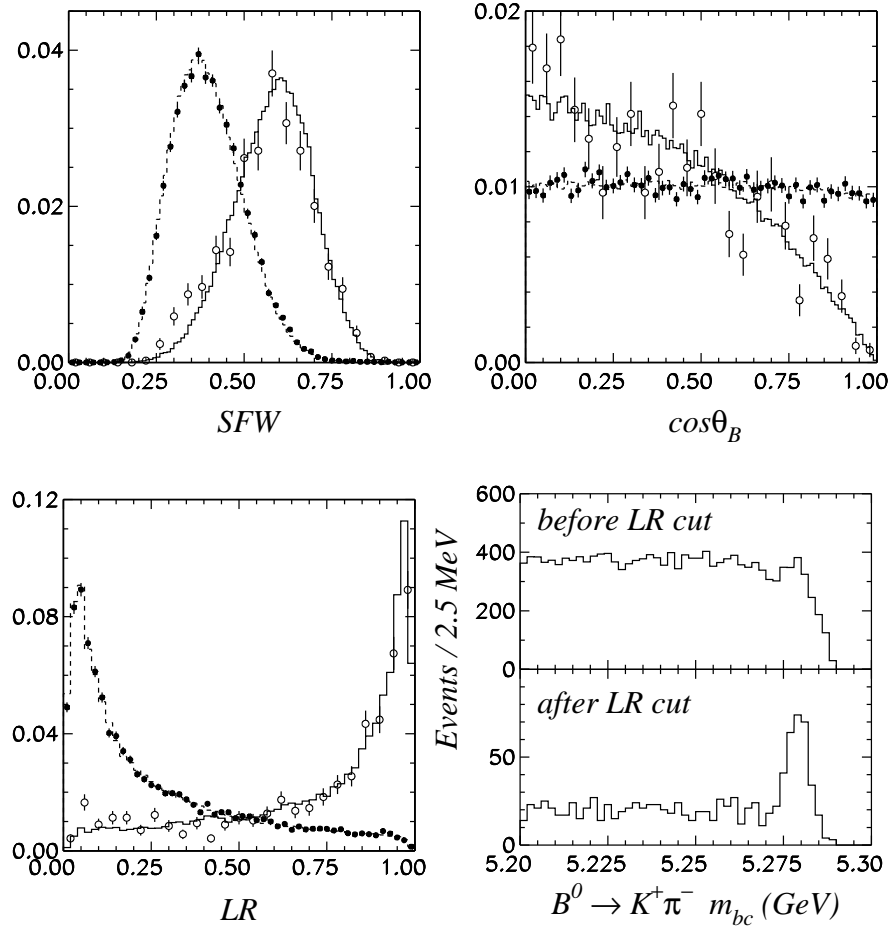


FIG. 2. Continuum suppression variables: SFW (top left), $\cos\theta_B$ (top right), and the combined likelihood ratio (bottom left). The solid curves are the signal PDFs derived from MC. The dashed curves are the continuum PDFs derived from sideband data. The open points are the $B^+ \rightarrow D^0\pi^+$, $D^0 \rightarrow K^-\pi^+$ data sample. The solid points are off-resonance data. The bottom right distribution is the beam constrained mass distribution for the $B^0 \rightarrow K^+\pi^-$ data sample before and after requiring the likelihood ratio cut $LR > 0.8$.

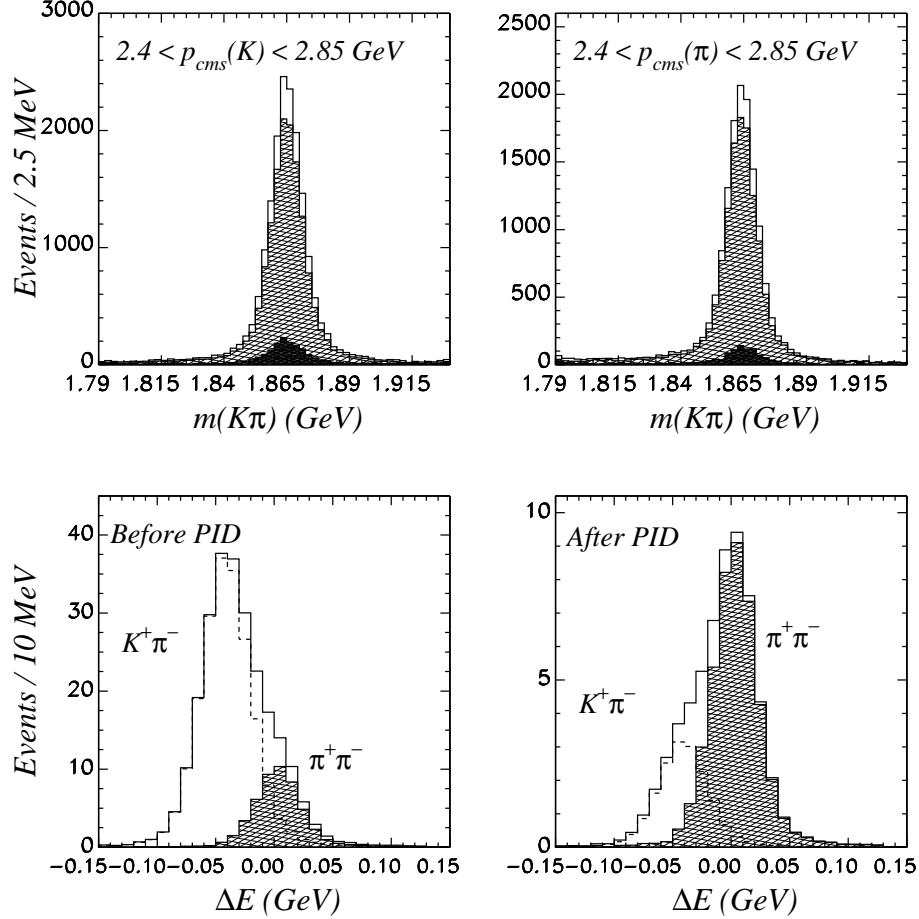


FIG. 3. The $D^{*+} \rightarrow D^0\pi^+$, $D^0 \rightarrow K^-\pi^+$ decay sample used to determine the PID efficiencies and fake rates, shown in the top row. The distribution on the left is the D mass distribution where the kaon daughter is required to have a similar momentum/ $\cos\theta$ distribution as the two-body $B \rightarrow hh$ decay daughters. The open histogram contains all candidates. The hatched histogram contains events where the kaon passes PID cuts. The solid histogram contains events where the kaon is mis-identified as a pion. The distribution on the right is the corresponding figure for the pion daughter. The bottom row shows the combined $B^0 \rightarrow K^+\pi^-$ and $\pi^+\pi^-$ MC ΔE distribution assuming a 4:1 $K^+\pi^-:\pi^+\pi^-$ production ratio. The distribution on the left is before PID cuts are applied. In the distribution on the right, both tracks are required to be identified as pions. The solid histogram is the sum of $K^+\pi^-$ and $\pi^+\pi^-$, the dashed histogram is the $K^+\pi^-$ component, and the hatched histogram is the $\pi^+\pi^-$ component.

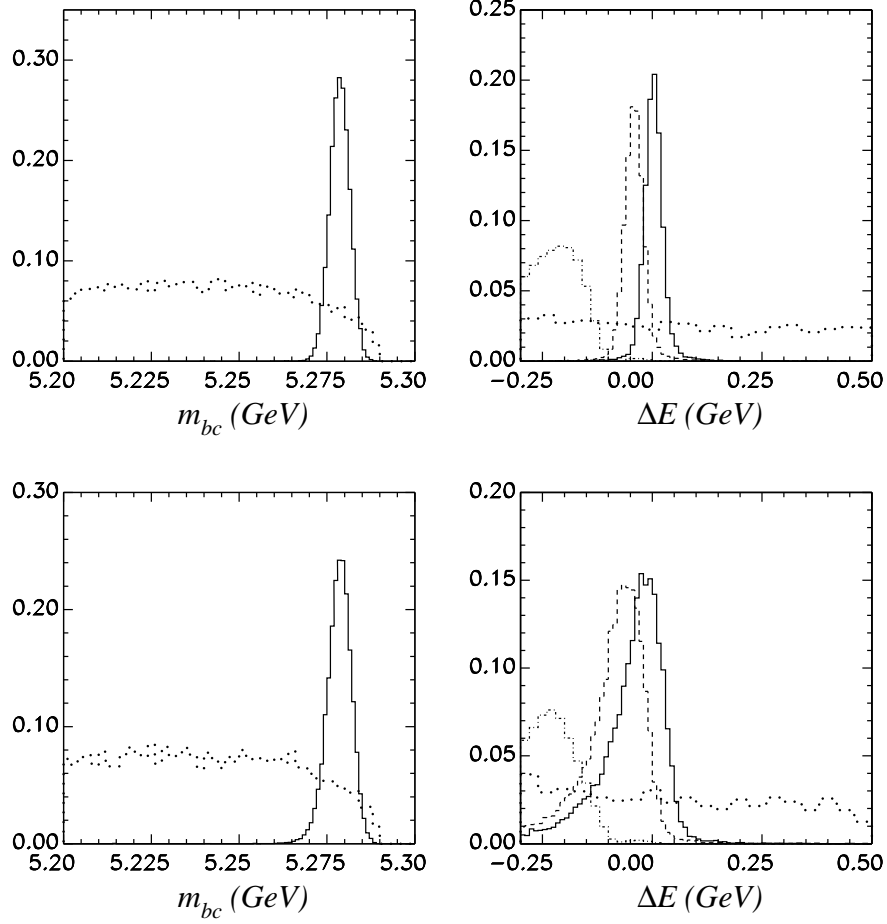


FIG. 4. Kinematic reconstruction variables m_{bc} (left) and ΔE (right) for $B^0 \rightarrow K^+\pi^-$ and $\pi^+\pi^-$ MC (top) and $B^+ \rightarrow K^+\pi^0$ and $\pi^+\pi^0$ MC (bottom). The solid histograms are $B^{0(+)} \rightarrow \pi^+\pi^{-(0)}$ MC. The dotted histograms are off-resonance data. The dashed histograms are for $B^{0(+)} \rightarrow K^+\pi^{-(0)}$ MC events, which are indistinguishable in the m_{bc} distribution but shifted by -45 MeV in ΔE due to pion mass assignment to the kaon track. The dot-dashed histograms represent background from multi-body charmless B meson decays.

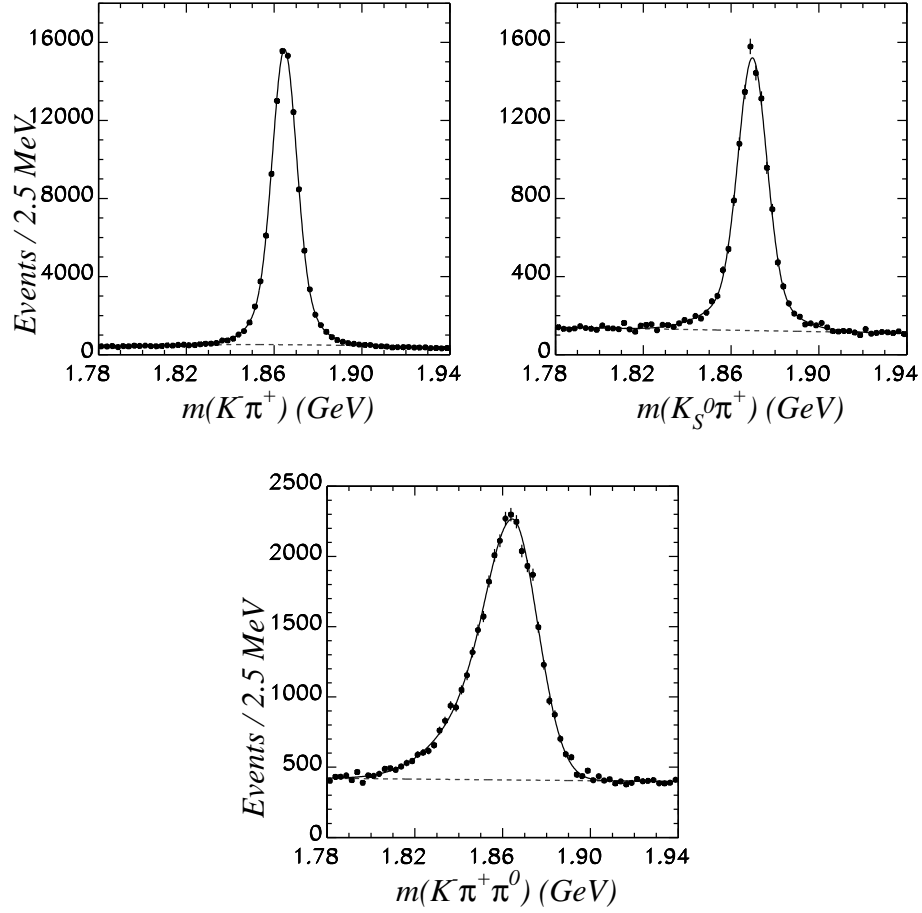


FIG. 5. Mass spectra for inclusive $D^0 \rightarrow K^-\pi^+$ (top left), $D^+ \rightarrow K_S^0\pi^+$ (top right), and $D^0 \rightarrow K^-\pi^+\pi^0$ (bottom) used to determine ΔE fit parameters. In each case, momentum cuts are placed on the D daughter particles to simulate the momentum of B daughter particles.

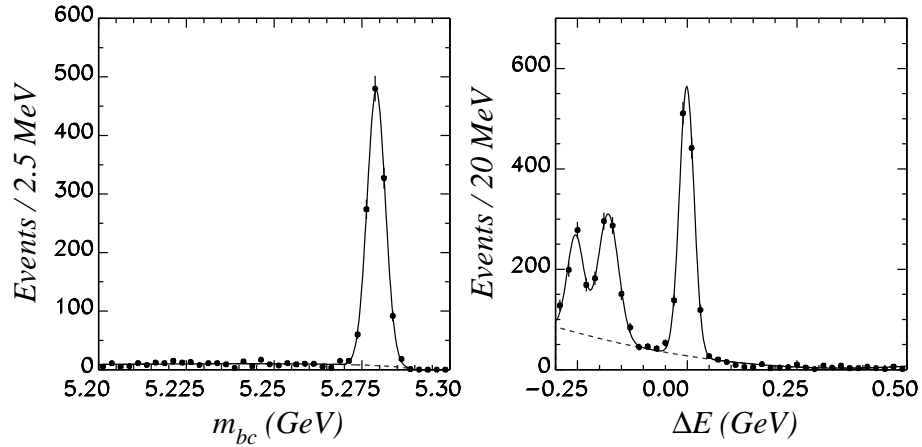


FIG. 6. The $B^+ \rightarrow D^0\pi^+$, $D^0 \rightarrow K^-\pi^+$ data sample used to determine m_{bc} (left) and ΔE (right) fit parameters. The ΔE distribution contains backgrounds from $B^0 \rightarrow D^0\pi^+\pi^-$.

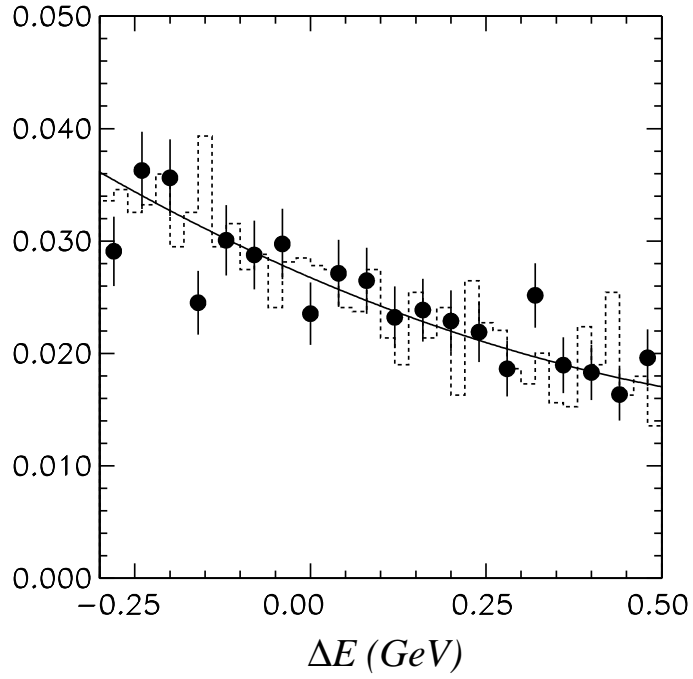


FIG. 7. The ΔE distribution for $B^+ \rightarrow K_S^0 \pi^+$ candidates in m_{bc} sideband data (dashed-histogram) compared to the same distribution in the m_{bc} signal window for off-resonance data (black circles). The solid curve is a second-order polynomial used to parameterize the shape.

TABLE I. Efficiencies to reconstruct the $B \rightarrow hh$ modes. Listed are the efficiencies for reconstruction, particle identification, continuum suppression, the final combined efficiencies, and products of efficiency times intermediate branching fraction.

| Mode | Rec. | PID | $q\bar{q}$ | Final | $\epsilon \times \text{B.F.}$ |
|---------------------|------|------|------------|-------|-------------------------------|
| $K^+\pi^-$ | 0.73 | 0.76 | 0.55 | 0.31 | 0.31 |
| $\pi^+\pi^-$ | 0.75 | 0.77 | 0.52 | 0.30 | 0.30 |
| K^+K^- | 0.71 | 0.74 | 0.38 | 0.20 | 0.20 |
| $K^+\pi^0$ | 0.43 | 0.86 | 0.39 | 0.14 | 0.14 |
| $\pi^+\pi^0$ | 0.46 | 0.88 | 0.39 | 0.16 | 0.16 |
| $K^0\pi^+$ | 0.53 | 0.88 | 0.68 | 0.32 | 0.11 |
| K^0K^+ | 0.51 | 0.86 | 0.38 | 0.17 | 0.06 |
| $K^0\pi^0$ | 0.34 | 1 | 0.69 | 0.23 | 0.08 |
| $\pi^0\pi^0$ | 0.31 | 1 | 0.41 | 0.13 | 0.13 |
| $K^0\bar{K}^0$ [28] | 0.37 | 1 | 0.54 | 0.20 | 0.04 |

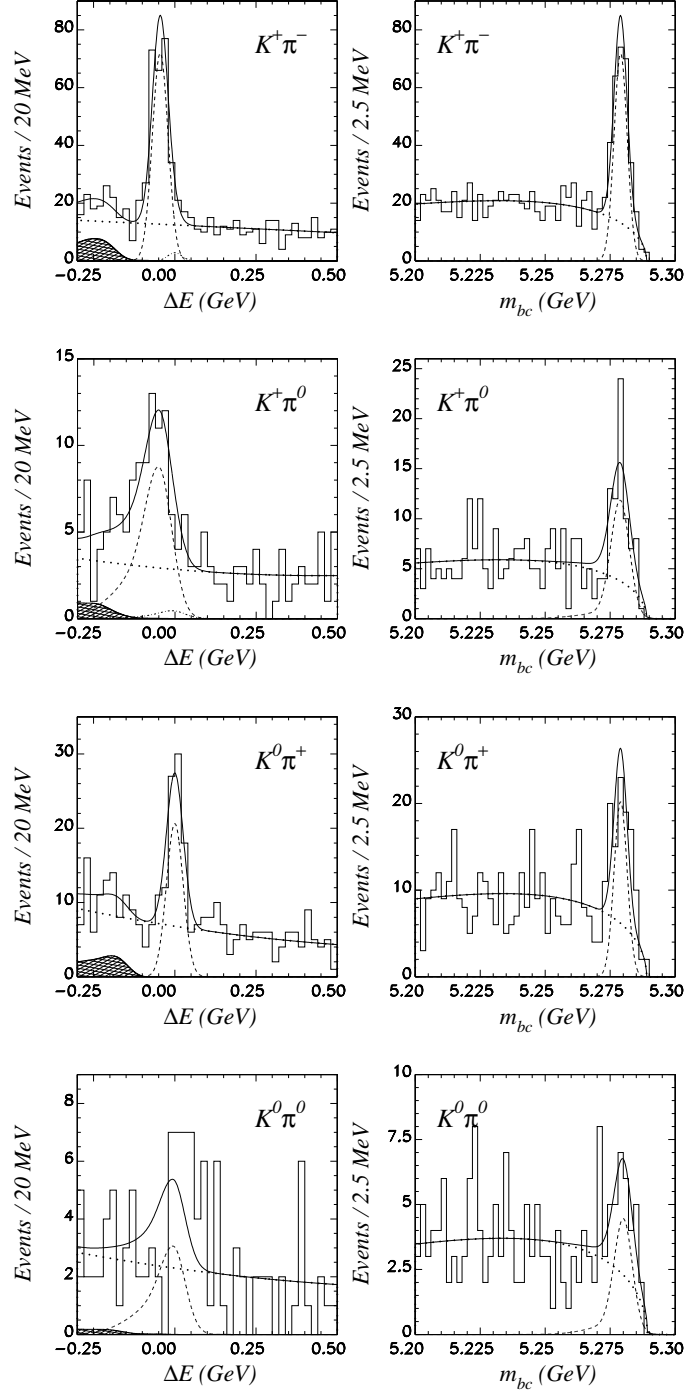


FIG. 8. The ΔE (left) and m_{bc} (right) fits to the $B \rightarrow K\pi$ event samples. The sum of the signal and background functions is shown as a solid curve. For the ΔE distributions, the dashed curve represents the signal component, the dotted curve represents the continuum background, and the hatched histogram represents the charmless B background component. For the $K^+\pi^-$ and $K^+\pi^0$ distributions, the crossfeed components from $\pi^+\pi^-$ and $\pi^+\pi^0$ are shown by dot-dashed curves centered 45 MeV above the signal components. For the m_{bc} distributions, the continuum background is represented by the dotted curve while the sum of signal, charmless B background, and crossfeed components is shown by the dashed curve.

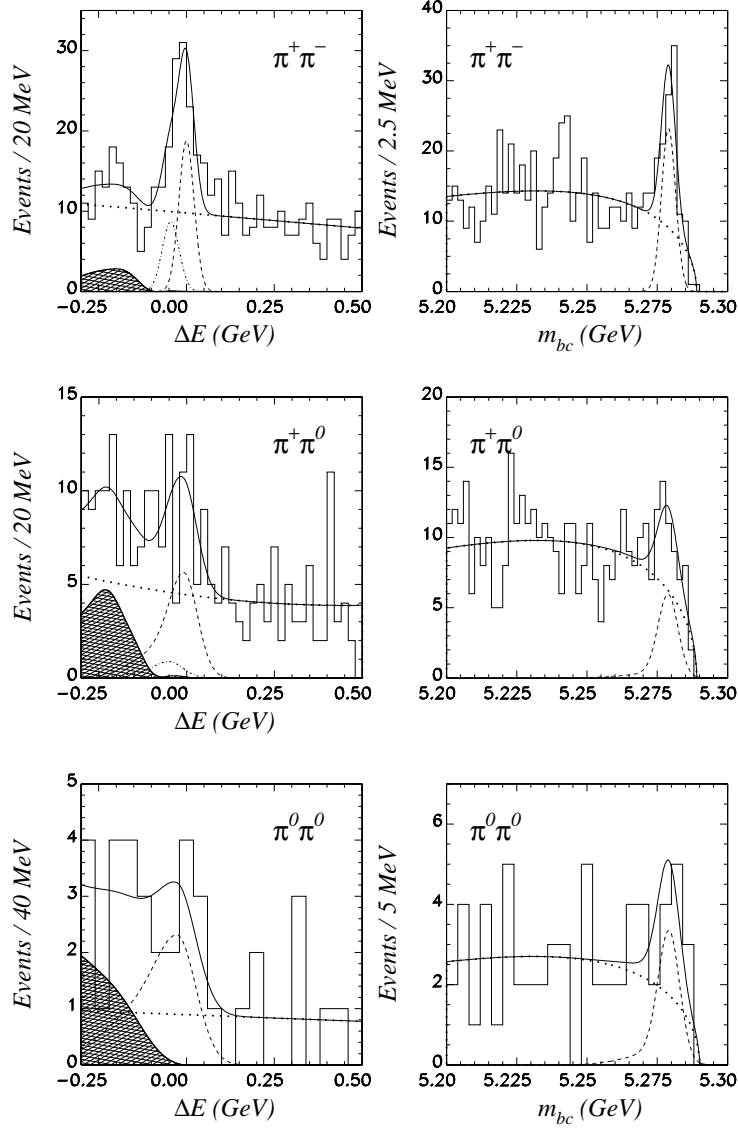


FIG. 9. The ΔE (left) and m_{bc} (right) fits to the $B \rightarrow \pi\pi$ event samples. The sum of the signal and background functions is shown as a solid curve. For the ΔE distributions, the dashed curve represents the signal component, the dotted curve represents the continuum background, and the hatched histogram represents the charmless B background component. For the $\pi^+\pi^-$ and $\pi^+\pi^0$ distributions, the crossfeed components from $K^+\pi^-$ and $K^+\pi^0$ are shown by dot-dashed curves centered 45 MeV below the signal components. For the m_{bc} distributions, the continuum background is represented by the dotted curve while the sum of signal, charmless B background, and crossfeed components is shown by the dashed curve.

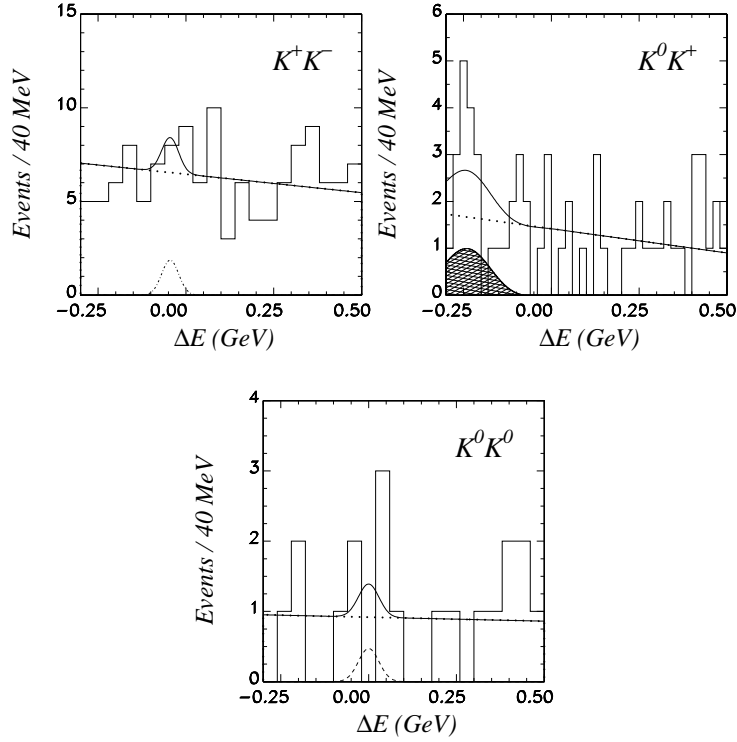


FIG. 10. The ΔE fits to the $B \rightarrow K\bar{K}$ event samples. The sum of the signal and background functions is shown as a solid curve, the dotted curve represents the continuum background. In the $B^0 \rightarrow K^+K^-$ distribution, the dot dashed curve represents the $K^+\pi^-$ crossfeed. In the $B^+ \rightarrow K_S^0 K^+$ distribution, the hatched histogram represents the charmless B background. In the $B^0 \rightarrow K_S^0 K_S^0$ distribution, the dashed curve represents the signal component.

TABLE II. Signal yields, significance above background, and branching fractions for $B \rightarrow hh$ modes assuming equal production fractions for neutral and charged B meson pairs. We report 90% confidence level upper limits for the $B^0 \rightarrow \pi^0\pi^0$ and $B \rightarrow K\bar{K}$ decays.

| | Yield | Sig. | B.F. ($\times 10^{-5}$) |
|----------------|-------------------------|------|---------------------------------|
| $K^+\pi^-$ | $217.6^{+18.6}_{-17.9}$ | 16.4 | $2.25 \pm 0.19 \pm 0.18$ |
| $K^+\pi^0$ | $58.5^{+11.3}_{-10.7}$ | 6.4 | $1.30^{+0.25}_{-0.24} \pm 0.13$ |
| $K^0\pi^+$ | $66.7^{+10.8}_{-10.1}$ | 7.6 | $1.94^{+0.31}_{-0.30} \pm 0.16$ |
| $K^0\pi^0$ | $19.8^{+8.3}_{-7.6}$ | 2.8 | $0.80^{+0.33}_{-0.31} \pm 0.16$ |
| $\pi^+\pi^-$ | $51.0^{+11.6}_{-10.9}$ | 5.4 | $0.54 \pm 0.12 \pm 0.05$ |
| $\pi^+\pi^0$ | $36.7^{+11.5}_{-10.8}$ | 3.5 | $0.74^{+0.23}_{-0.22} \pm 0.09$ |
| $\pi^0\pi^0$ | $12.5^{+6.2}_{-5.5}$ | 2.4 | < 0.64 |
| K^+K^- | $0^{+3.2}_{-0}$ | 0 | < 0.09 |
| K^0K^+ | $0^{+2.0}_{-0}$ | 0 | < 0.20 |
| $K^0\bar{K}^0$ | $0.9^{+2.9}_{-0.9}$ | 0 | < 0.41 |

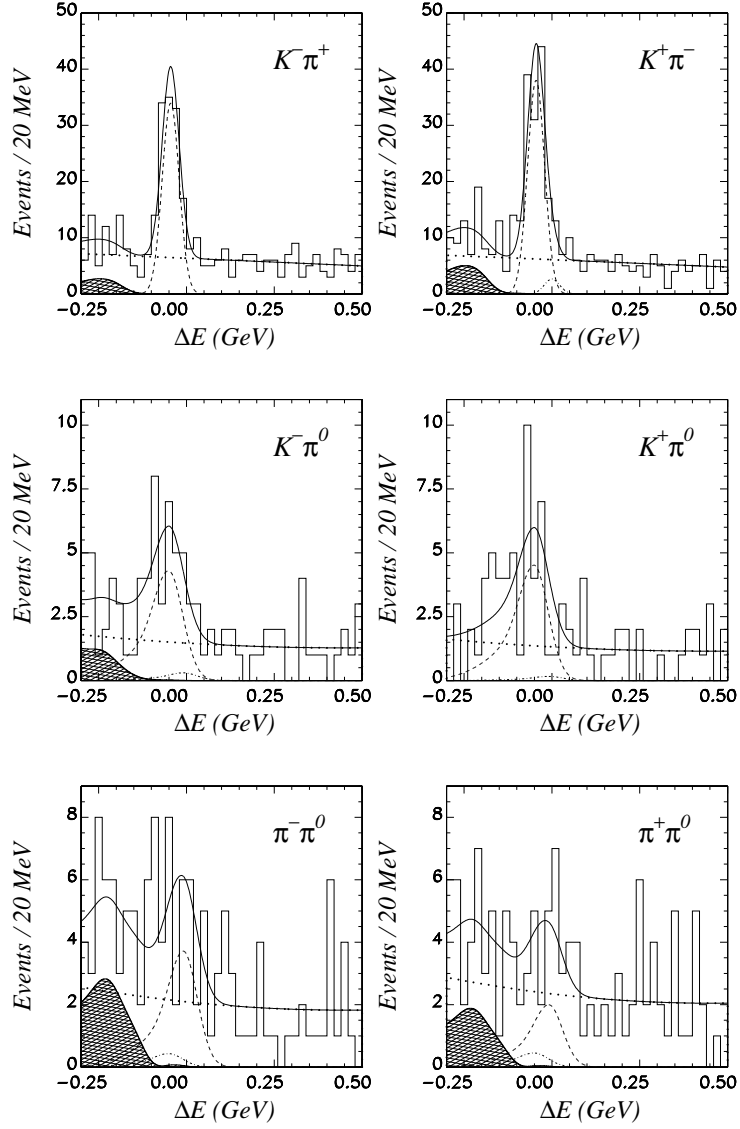


FIG. 11. The ΔE distributions for \bar{B} (left) and B (right) candidate decays to flavor-specific final states. The sum of the signal and background functions is shown as a solid curve. The dashed curve represents the signal component, the dotted curve represents the continuum background, and the hatched histogram represents the charmless B background component. The crossfeed components are shown by dot-dashed curves centered 45 MeV from the signal components.

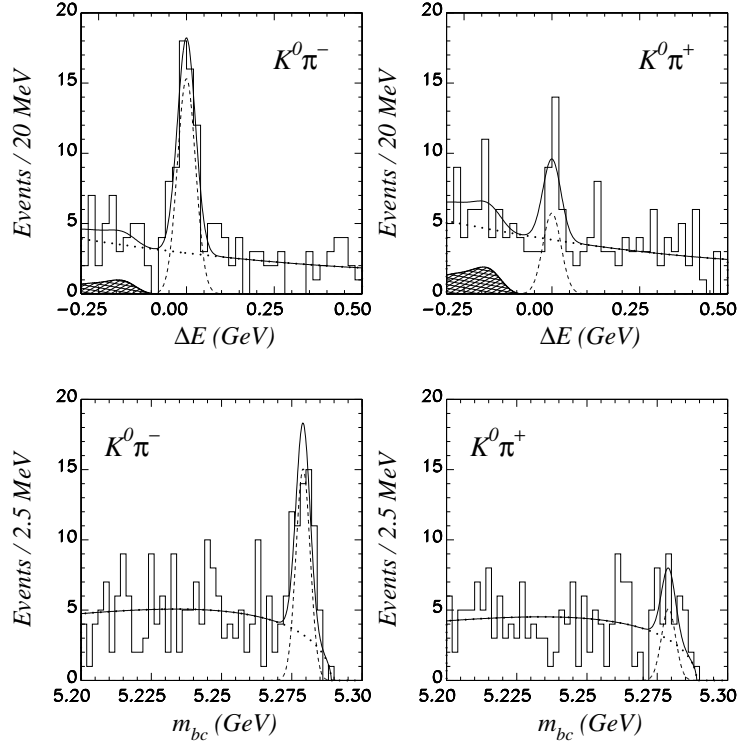


FIG. 12. Distributions for $B^\mp \rightarrow K_S^0 \pi^\mp$. The top row contains ΔE distribution for \bar{B} (left) and B (right) candidates. The corresponding m_{bc} distributions are shown in the bottom row. The sum of the signal and background functions is shown as a solid curve. The dashed curve represents the signal component, the dotted curve represents the continuum background, and the hatched histogram represents the charmless B background component.

TABLE III. Ratios of partial widths among the various $B \rightarrow K\pi$ and $\pi\pi$ final states assuming equal production fractions for neutral and charged B meson pairs. The ratios of branching fractions are converted to ratios of partial widths using $\tau^+/\tau^0 = 1.091 \pm 0.027$ [34].

| Γ_2/Γ_1 | |
|---|--|
| $\pi^+\pi^-/K^+\pi^-$ | $0.24^{+0.06}_{-0.05} \pm 0.02$ |
| $2K^+\pi^0/K^0\pi^+$ | $1.34 \pm 0.33^{+0.15}_{-0.14}$ |
| $(\tau^+/\tau^0)K^+\pi^-/K^0\pi^+$ | $1.27^{+0.22}_{-0.23} \pm 0.10$ |
| $K^+\pi^-/2K^0\pi^0$ | $1.41^{+0.56}_{-0.60}^{+0.28}_{-0.27}$ |
| $(\tau^+/\tau^0)\pi^+\pi^-/2\pi^+\pi^0$ | $0.40 \pm 0.15 \pm 0.05$ |
| $(\tau^+/\tau^0)\pi^0\pi^0/\pi^+\pi^0$ | < 0.83 (90% C.L.) |

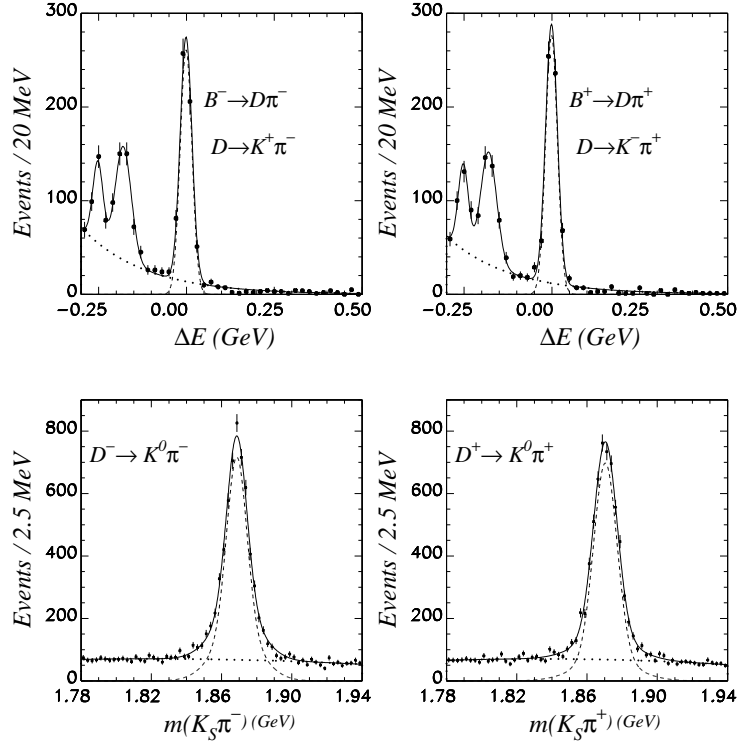


FIG. 13. Control samples for the $B^{\mp} \rightarrow K_S^0 \pi^{\mp} \mathcal{A}_{CP}$ measurement. The top row contains the ΔE distributions for $B^- \rightarrow \bar{D}^0 \pi^-$, $\bar{D}^0 \rightarrow K^+ \pi^-$ on the left and the charge conjugate decay on the right after applying identical PID and continuum suppression cuts as for the $K_S^0 \pi^{\mp}$ analysis. The bottom row contains inclusive $D^- \rightarrow K_S^0 \pi^-$ (left) and $D^+ \rightarrow K_S^0 \pi^+$ (right) mass spectra after making momentum cuts on the D daughter particles to simulate the momentum of B daughter particles.

TABLE IV. Partial-rate asymmetries. Listed are the number of signal events for each final state, the \mathcal{A}_{CP} values with errors, and their 90% confidence intervals, listed on the following line. In the $K^{\mp} \pi^{\pm}$ final states, the asymmetry is corrected for the dilution due to double mis-identification.

| Mode | $N(\bar{B})$ | $N(B)$ | \mathcal{A}_{CP} (90% C.L.) |
|---------------------|------------------|------------------|--|
| $K^{\mp} \pi^{\pm}$ | 102.8 ± 12.6 | 115.0 ± 13.3 | $-0.06 \pm 0.09^{+0.01}_{-0.02}$ $-0.21 : 0.09$ |
| $K^{\mp} \pi^0$ | 28.7 ± 7.8 | 30.1 ± 7.7 | $-0.02 \pm 0.19 \pm 0.02$ $-0.35 : 0.30$ |
| $K_S^0 \pi^{\mp}$ | 49.5 ± 8.4 | 18.6 ± 6.3 | $0.46 \pm 0.15 \pm 0.02$ $0.19 : 0.72$ |
| $\pi^{\mp} \pi^0$ | 24.2 ± 8.4 | 13.0 ± 7.3 | $0.30 \pm 0.30^{+0.06}_{-0.04}$ $-0.23 : 0.86$ |

TABLE V. Tests of detector based asymmetries. The first row is based on an inclusive track sample with $2.4 \text{ GeV} < p < 2.85 \text{ GeV}$ in the center of mass frame. The following two rows are the asymmetries in the same sample after applying particle ID. The fourth row is the asymmetry for inclusive D meson decays to high momentum $K^+\pi^-$, $K^+\pi^-\pi^0$, and $K_S^0\pi^+$ final states. The fifth and sixth rows are the asymmetries in the m_{bc} sideband and the $B^{+(0)} \rightarrow D^{0(-)}\pi^+$ data sample before and after the LR cut is applied.

| test sample | \mathcal{A}_{CP} | |
|--------------------------|-----------------------------------|--------------------|
| high p tracks | $(-3.6 \pm 0.3) \times 10^{-3}$ | |
| with K pid | $(-3.2 \pm 0.5) \times 10^{-3}$ | |
| with π pid | $(-3.7 \pm 0.3) \times 10^{-3}$ | |
| high p D decays | $(-2 \pm 3) \times 10^{-3}$ | |
| | before LR cut | after |
| m_{bc} sideband | $(-0.07 \pm 0.17) \times 10^{-3}$ | 0.01 ± 0.05 |
| $B \rightarrow D\pi^\mp$ | -0.045 ± 0.025 | -0.055 ± 0.027 |